coatings

MDPI

Article

Synthesis of Two Structurally Different MgO Films Containing Dioxygen Species: Dioxygen Embedded at Grain Boundaries, and as Components of a Superfilled Rock Salt Structure

Dieter Fischer [1,*], Dejan Zagorac [2], Kathrin Küster [1] and Johann Christian Schön [1]

[1] Max Planck Institute for Solid State Research, Heisenbergstr. 1, 70569 Stuttgart, Germany
[2] Institute of Nuclear Sciences Vinca, Materials Science Laboratory, University of Belgrade, 11000 Belgrade, Serbia
* Correspondence: d.fischer@fkf.mpg.de

Abstract: Magnesium oxide films prepared as monolayer, amorphous, and epitaxial films have different properties such as semiconducting, ferromagnetic, and dielectric behavior, respectively. Understanding the variation in these properties requires detailed information about the atomic structure of the different MgO films. In the present study, one important synthesis method, ballistic deposition, is studied, and the influence of the deposition temperature on the resulting atomic structure of the films is analyzed in detail, employing XRD, SEM, EDX, XPS, and Raman scattering. At −190 °C, compact, light-yellow films are obtained, which consist of small crystallites adopting the rock salt structure with an excess of oxygen at the grain boundaries. However, at 25 °C, nearly stoichiometric, white, columnar films exhibiting a superfilled rock salt structure are grown. In the first case, dioxygen species are formed by connecting the oxygen shells of adjacent small crystalline grains, and in the second case such species appear due to the partial occupation of tetrahedral sites in the rock salt structure. These observations should open new prospects of fine-tuning the properties of MgO films and enhance the performance of devices employing such films.

Keywords: magnesium; oxides; thin film; crystal structure; dioxygen species; defects; X-ray diffraction

Citation: Fischer, D.; Zagorac, D.; Küster, K.; Schön, J.C. Synthesis of Two Structurally Different MgO Films Containing Dioxygen Species: Dioxygen Embedded at Grain Boundaries, and as Components of a Superfilled Rock Salt Structure. *Coatings* **2024**, *14*, 1563. https://doi.org/10.3390/coatings14121563

Academic Editor: Alberto Palmero

Received: 29 October 2024
Revised: 26 November 2024
Accepted: 10 December 2024
Published: 13 December 2024

1. Introduction

Magnesium oxide is a colorless ceramic with a band gap of 7.8 eV [1]. It is highly thermodynamically stable and has a very low free energy of formation at standard conditions (ΔG = −568.6 kJ/mol) [2]. Only one bulk polymorph of MgO is known, which crystallizes in the rock salt structure [3]. Considering thin MgO films, not only the rock salt structure but also the metastable wurtzite structure is found in films up to 1 nm thick, and some stacking fault structures are obtained in stacks up to about 10 nm thick [4]. In addition, studies of ZnO/MgO superlattices reveal the wurtzite structure in MgO layers up to 1.5 nm thick, stabilized by a spontaneous interfacial mixing [5]. Investigations of epitaxial MgO films grown on sapphire substrates indicate an intermediate structure between the wurtzite and the rock salt structure of MgO at the interface [6]. The observed structural arrangement is consistent with the ionic analog of the hexagonal BN structure (the so-called 5–5-type) [7], supported by predictions of the structure candidates for MgO layers of an Al_2O_3 substrate [8]. Theoretical calculations suggest many other structure candidates for MgO, exhibiting, e.g., the zinc blende, TiP, and β-BeO structures [9,10].

Magnesium oxide is used for numerous applications as an insulator and refractory component as well as for catalytic, biological, agricultural, and therapeutic applications [11]. In particular, the (photo)catalytic applications of MgO nanoparticles for organic reactions (synthesis, transformation, degradation) have developed into a broad field in recent decades [12,13]. In many cases, MgO films, which have been extensively studied for more than 40 years, are deposited on metal [14,15], oxide [16,17], and semiconductor [18,19]

substrates. Epitaxial films (2 to 250 nm thick) are grown on SiC and GaN substrates by molecular beam epitaxy (MBE) for substrate temperatures between 25 and 650 °C [18,20,21]. The MBE is performed using an oxygen plasma together with a Mg source, and the MgO(111) epitaxial growth, with adjusted growth rates, is achieved for up to 250 nm thick films [18]. Micrometer-thick, highly textured films with columnar grain morphology (on Si, SiO_2, and metal substrates) are grown at near room temperature by electron beam deposition under oxygen pressure using MgO sources [22–24]. In addition, amorphous and polycrystalline films have been obtained by pulsed laser deposition (PLD) [25,26], chemical vapor deposition (CVD) [27,28], and sputtering [29,30]. For the PLD and sputtering experiments, both MgO and Mg targets are used, as well as various organometallic precursors for the CVD processes. The crystallinity of the actual films is mostly a function of the substrate temperature. Thus, the CVD and sputtering techniques yield amorphous films for depositions at room temperature [27,30] and nearly epitaxial ones at substrate temperatures above 500 °C (CVD) [27,28] and at about 750 °C (sputtering) [31]. In PLD experiments, the conditions resulting in the degree of crystallinity achieved in the MgO films are more complex and the outcome depends on the substrate temperature as well as on the oxygen pressure and the laser fluence [26,32]. Thus, MgO(111) and (100) textured films are grown on various substrates such as Si, SiO_2, and sapphire between 25 and 850 °C with film thicknesses ranging from one to a few hundred nanometers.

An important application of MgO films is as a buffer layer or oxide barrier in thin film superconductors, semiconductors, and ferroelectrics [1]. The MgO films (2 to 40 nm) are used in multifunctional metal oxide heterostructures on Si and SiC substrates and are deposited by the MBE method [19,21,33]. Here, the MgO(111) films grow on SiC(0001) substrates in a quasi-2D multi-layer manner, resulting in a 3D film termination with {100} facets [20]. In general, film growth by MBE has been studied experimentally in detail as a function of substrate temperature and Mg and molecular O_2 fluxes. Different growth regimes are delineated for GaN(0001) and amorphous SiO_2 substrates by a critical substrate temperature for Mg re-evaporation and the Mg:O flux ratio [34]. Furthermore, the variables of the MBE growth process have been analyzed by Monte Carlo and neural networks-based meta-models [35,36].

The homoepitaxial growth process of MgO films on MgO(001) substrates has also been studied experimentally [37] as well as theoretically [38,39]. The adsorption and diffusion of Mg, O, and O_2 on the surface during the process are analyzed by ab initio calculations based on the density functional theory (DFT) method. The critical influence on the growth under the O_2 atmosphere is found to be the surface concentration of point defects [38]. Additionally, the diffusion mechanism of a MgO admolecule is also investigated by molecular dynamics (MD) simulations [40,41]. Experimentally, the homoepitaxial film growth is investigated by fast Auger spectroscopy, among other methods, for films with a thickness of a few tens of nanometers, which are deposited from separate beams of Mg and activated oxygen in a substrate temperature range of 450 to 750 °C. The results show that at elevated temperatures (ca. 750 °C), MgO grows homoepitaxially via the step-flow growth mechanism, and excess oxygen is not adsorbed on the surface nor incorporated into the crystal [37].

In addition, MgO films (ca. 100 nm thick) have been found to exhibit unexpected ferromagnetism at room temperature [42]. These films are prepared by PLD and sputtering techniques on Si substrates [43,44]. The ferromagnetic ordering is a function of the film thickness [43] and the deposition temperature [44] as well as the oxygen pressure during deposition [45]. The ferromagnetism of MgO films has been attributed to Mg cation vacancies [42,46], but the possible origin of the d^0 ferromagnetism is not very clear. Recently, new 2D monolayer materials, including MgO, have been reported which have attracted enormous interest due to their optical and electronic properties. For example, the MgO graphene-like monolayer (analogous to a monolayer of the 5–5-structure [7]) shows a non-magnetic, semiconducting behavior [47–49].

As the wealth of the above observations shows, the synthesis of MgO films has been extensively studied. Nevertheless, many questions remain. For one, the film growth, which is a combination of 2D and 3D modes, is remarkably varied, showing different regimes with an onset of the deposition rate at low (>5 × 10^{-7} mbar) and a reduction in the rate at high oxygen pressures (>5 × 10^{-6} mbar) [34], respectively. Moreover, isolated Mg atoms and molecular oxygen are only loosely bound to the surface, and thus can be easily evaporated at room temperature [38]. Thus, above a critical temperature (250 °C), film growth starts only when both components, Mg and oxygen, hit the surface in such a way that reactions can quickly take place. These results are evident for films with deposition rates up to a few nanometers per minute. Otherwise, at room temperature, a self-shadowing effect with void formation is suggested for high Mg fluxes (deposition rates: 6–12 nm/min.) forming porous films [34]. For the ballistic deposition region (high deposition rates at low temperatures), the films prepared by electron beam deposition using MgO targets under oxygen pressure have not yet been studied in detail [23,24]. Almost exclusively, the texture of these films has been characterized with respect to their buffer layer properties. Therefore, we decided to study MgO films deposited directly from the elements, magnesium and oxygen, with ballistic deposition rates at substrate temperatures of 25 and −190 °C. In the ballistic deposition regime, the incoming atoms/molecules are typically transferred to the substrate in a straight line and are incorporated in the immediate vicinity of their original landing site (cf. [22]). An interesting point is the influence of the high deposition rates on the behavior of the weakly bonded adatoms (magnesium and oxygen) with regard to the film structure formed. A key issue here is the implementation of two separate beams of magnesium and oxygen to ensure the synthesis of MgO directly from the elements. Our experiments yield micrometer-thick MgO films that we characterize by scanning electron microscopy (SEM), energy-dispersive X-ray spectroscopy (EDX), X-ray photoelectron spectroscopy (XPS), X-ray diffraction (XRD), and Raman measurements, with the analysis supported by ab initio calculations.

2. Materials and Methods

The MgO films were synthesized using magnesium (99.99% Mateck GmbH, Jülich, Germany) evaporated from a PBN crucible by an effusion cell (Dr. Eberl MBE-Komponenten GmbH, Weil der Stadt, Germany) at 400 and 420 °C, together with oxygen (O_2, purity 5.0; Westfalen AG, Münster, Germany) at a mass flow of 1 sccm, which was passed through a microwave plasma cell (electron-cyclotron-resonance (ECR) Plasma source, Tectra GmbH, Frankfurt/M, Germany) operating at 2.45 GHz and 60 mA. Both cells were mounted at an angle of 22° to the substrate normal via fixed ports of the vacuum chamber. As deposition temperatures, both room temperature (25 °C) and the experimentally well-controllable temperature of liquid nitrogen (−190 °C) were chosen. The substrates were mounted on a copper holder that was attached to two tubes so that the holder could be cooled to −190 °C with liquid nitrogen. The films were deposited on sapphire substrates (epitaxially polished, orientation (0001), CrysTec, GmbH, Berlin, Germany) for a period of 3 h at substrate temperatures of −190 and 25 °C. During the process, the pressure in the vacuum chamber was 2.5 × 10^{-5} mbar of oxygen. This oxygen pressure results in a flux of 1.5 × 10^{16} oxygen/cm^2·s, and the operating temperature of the Mg effusion cell results in a sublimation rate of 2 × 10^{18} atoms/cm^2·s of magnesium at the cell opening. A flux reduction of 10^{-3} is expected at the distance of 15 cm from the effusion cell to the substrate [50], resulting in a magnesium flux of approximately 2 × 10^{15} atoms/cm^2·s at the growth surface. Thus, a 10-fold excess of oxygen is used for the deposition process. After deposition, the samples were transferred directly from the deposition chamber to an X-ray diffractometer equipped with a Raman microscope for Raman measurements under vacuum.

The MgO single crystals (5 × 5 × 1 mm, polished, (100) orientation) used for reference measurements were purchased from CrysTec GmbH (Germany).

The X-ray powder patterns were measured with a θ/θ-diffractometer (D8-Advance, Bruker AXS, Karlsruhe, Germany) at room temperature with a Goebel mirror (Cu-Kα) inside a vacuum chamber (ca. 10^{-7} mbar) in reflection mode using an area sensitive detector (Vantec-500, Bruker AXS). The structures were refined on integrated patterns by the Rietveld method using the TOPAS software (TOPAS V6, Bruker AXS [51]) with R-values between $3.4 < R_p < 5.9$. From the profile shape analysis (TOPAS), the crystallite sizes were calculated using the double-Voigt approach and the Lvol-1B values are given in Table 1 as λ. The preferred orientation was modeled with a preferred direction using the March-Dollase approach. The atomic displacement was refined using the isotropic temperature factor B_{eq}. The X-ray difference maps shown (reflecting the electron density) were obtained by combining the difference in the experimental and calculated structure factor amplitudes with the calculated phases [52]. Crystal structures were visualized using the Diamond software package (version 4.4.1; Crystal Impact GbR, Bonn, Germany) [53].

A laser-microscope Raman spectrometer (iHR 550 spectrometer; BXFM microscope, Horiba GmbH, Oberursel, Germany) with confocal geometry and a Peltier-cooled CCD camera (Synapse) was used for Raman measurements. The incident laser beam (532 nm at 20 mW) passed through a window in a vacuum chamber (ca. 10^{-7} mbar) and was focused on the samples by an objective lens (magnification ×100) [54]. The resolution of the spectrometer (three-grating 1800 L/mm) was about 1 wavenumber. Measurements were started at 70 cm^{-1} up to 1900 cm^{-1} at −190 °C.

Scanning electron microscopy (SEM) images were taken with a field emission microscope (Merlin, Carl Zeiss GmbH, Oberkochen, Germany) using an accelerating voltage of 2–5 kV and an Everhart-Thornley (SE) detector at room temperature. Samples were transferred to the microscope in an argon atmosphere using a custom-built transfer chamber. The EDX (energy dispersive X-ray) elemental analysis, operating at 3 and 10 kV with an Oxford Instruments detector (Ultim Max and Extreme, Oxford Instruments NanoAnalysis, Wiesbaden, Germany), provides information from the film depth down to 150 nm and 1500 nm, respectively. From the film thicknesses of the samples (measured from the SEM images), the deposition rates were determined to be 24–36 nm/min, which is approximately 1 ML/s (thickness of a ML: 0.5 nm).

A Kratos AXIS ULTRA (Kratos Analytical Ltd., Wharfside, Manchester, UK) with monochromatic Al-K_α radiation (1486.6 eV) was used for XPS measurements at room temperature with a base pressure in the low 10^{-10} mbar range. The samples were mounted on a sample holder with double sided sticky tape and transferred to the XPS system under argon atmosphere. Survey scans and detail scans were acquired with a pass energy of 80 eV and 20 eV, respectively. A charge neutralizer was used for compensating the surface charges and the C 1s signal was set to 284.8 eV (adventitious carbon) for binding energy calibration [55]. Argon ion sputtering was performed with a raster-scanned argon ion beam using a MiniBeam III (Kratos Analytical) for 10 min with an energy of 4.0 keV. The sputter rate is roughly 0.7 nm/min calibrated on SiO_2 on Si. The XPS analysis provides information from the film depth of 1 to 5 nm. Casa XPS [56] was used for data analysis and peak fitting. For peak fitting, a Shirley background was subtracted and an LA line shape, which is a numerical convolution of a Lorentzian and a Gaussian function, was used. For quantification, the Scofield cross sections [57] as implemented in Casa XPS were used. However, quantification in XPS is always prone to errors; therefore, absolute values might differ, but relative values for similar samples can be extracted.

The ab initio calculations were performed using the CRYSTAL17 code, based on the linear combination of atomic orbitals [58]. The crystallographic analysis was executed using the KPLOT package [59]. The full structural optimizations were carried out using analytical gradients, and the subsequent phonon calculations were based on analytical first and numerical second derivatives [60]. The LO-TO splitting at the Γ-point was calculated within the framework of the coupled perturbed Kohn–Sham method [61]. Ab initio calculations were performed using Hartree–Fock (HF) and Density Functional Theory (DFT) methods, employing the B3LYP functional (Becke's three-parameter functional in combination with

the correlation functional of Lee, Yang, and Parr) [62] and the generalized gradient approximation (GGA) with the PBE (Perdew, Burke, and Ernzerhof) functional [63]. It is useful to choose several different ab initio methods to obtain some feeling for the quantitative validity of the theoretical data [64]. All electron basis sets (AEBS) were used, a [4s3p1d] basis set in the case of magnesium [65], and a [4s3p] basis set in the case of oxygen [66].

3. Results

The MgO films were synthesized by deposition of Mg together with oxygen activated by a microwave plasma on sapphire substrates at constant substrate temperature (T_S) of 25 and −190 °C with deposition rates of 24 and 36 nm/min, respectively. These deposition rates are in the ballistic region for the deposition of MgO films, where typical growth rates of tens to hundreds of nm/min are observed [23,24].

3.1. Electron Microscopy

Deposition at −190 °C yields light-yellow films with thicknesses of approx. 6 µm. The SEM images (see Figure 1, all taken at 25 °C) show layer-by-layer grown, dense, compact films (see Figure 1e), which are cracked (piece sizes: tens of microns) and have slight flat hills on the surface (1–2 µm in diameter) that look like stuck-on bubbles (see Figure 1a). At higher magnification (see Figure 1c), a smooth surface with an irregular structure on the nanometer scale (ca. 10 nm) can be seen. The MgO films deposited at 25 °C are white with thicknesses of approx. 4 µm (once a black film was also obtained). These films have a granular surface morphology on the nanometer scale and consist of side-by-side grown rectangular columns oriented nearly perpendicular to the surface (cf. SEM images in Figure 1b,f). The individual columns are closely intergrown and their diameters vary from 20 to 40 nm. The tops of the columns form a roofing tile-like rough surface (see Figure 1d). This film morphology is well known from MgO buffer layers for superconducting films prepared under ballistic deposition conditions on metal substrates at room temperature [24]. The SEM images already demonstrate that the growth of MgO films for different substrate temperatures leads to very different film morphologies.

3.2. X-Ray Diffraction

The films deposited, at both substrate temperatures, are polycrystalline and the X-ray powder patterns are shown in Figure 2. The X-ray powder pattern of the film deposited at −190 °C shows broad reflections with intensities corresponding to those expected from MgO crystallizing in the rock salt structure. The rock salt structure can be described as a face-centered cubic lattice (fcc) of magnesium with oxygen occupying every octahedral void or vice versa (*Fm*-3*m*, Mg: 4a (0,0,0), O 4b (½,½,½)). The pattern of the film deposited at 25 °C shows much sharper reflections whose positions are also consistent with the rock salt structure. However, the intensities are very different from the expected ones, and only the (111) reflection at ca. 37° in 2θ shows a texture-related intensity deviation (visible on X-ray detector images). The corresponding Rietveld refinements reveal, for the Mg films deposited at −190 °C, the rock salt structure with very small crystallite sizes (λ) of 3 nm, together with a lattice constant increased by about 1% compared to the bulk material (cf. Table 1 and Figure S1 in Supplementary Materials). For the films deposited at 25 °C, no satisfactory refinement of the rock salt structure is possible. Employing different texture models does not lead to a significant improvement, especially the oxygen site cannot be refined satisfactorily.

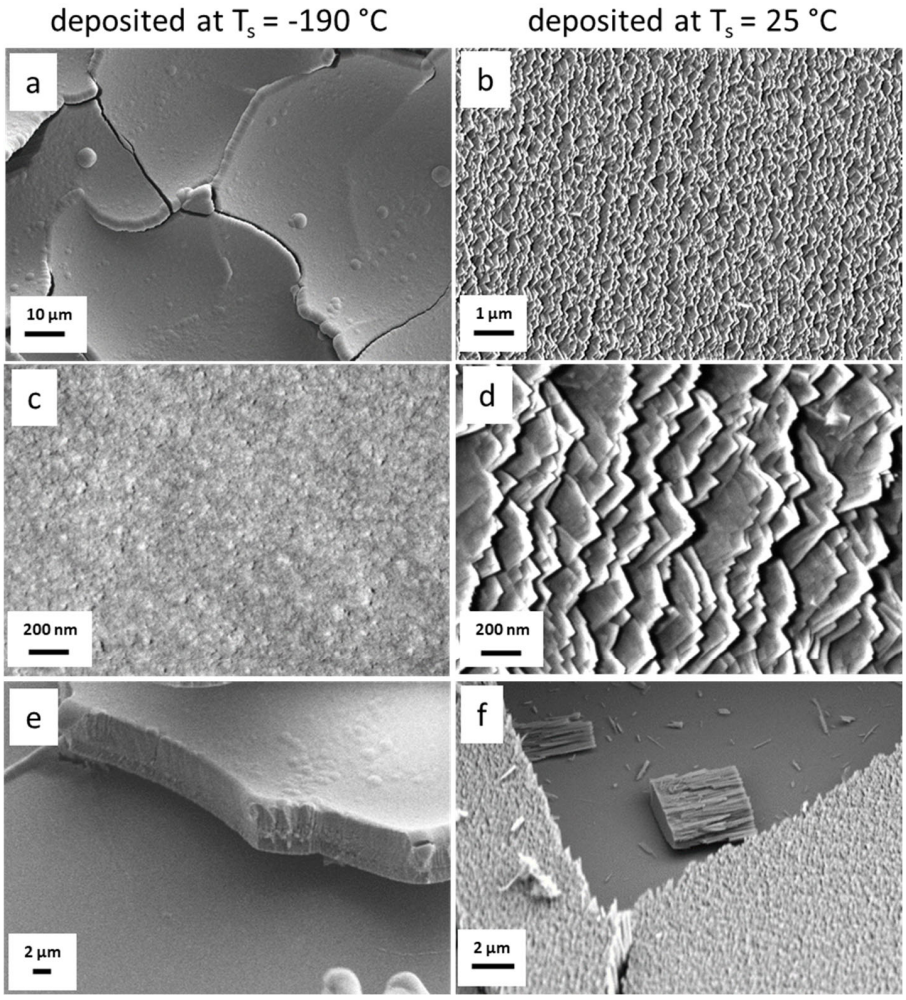

Figure 1. SEM images of the surface of the MgO films deposited at −190 °C and 25 °C with overview images in (**a**,**b**) and with higher magnification in (**c**,**d**). Film areas scratched by a needle to visualize the cross section of the films are shown in (**e**,**f**); (**e**: 6.6 µm thick and **f**: 4.4 µm thick films); (all images are taken at 25 °C).

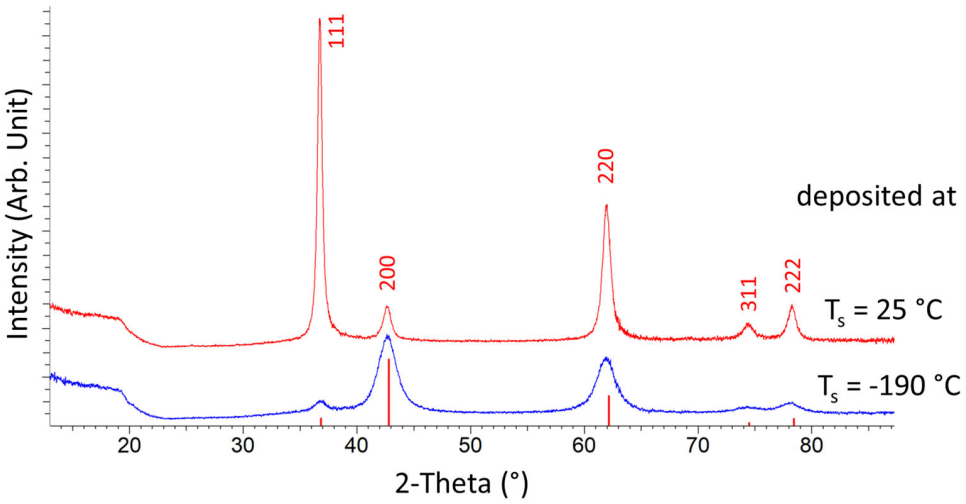

Figure 2. X-ray powder patterns of MgO films deposited at 25 °C (red curve) and −190 °C (blue curve). Patterns are vertically shifted for better visualization. All measurements were performed at 25 °C. The XRD line pattern of MgO (rock salt structure) is shown as red bars, including Miller indices hkl. Note the difference in the relative heights of the reflections when comparing the two films.

Table 1. Rietveld refinement data based on X-ray powder diffraction of MgO films deposited at −190 and 25 °C (T_S), including refined data of MgO powder and reference data of a MgO crystal * (all measurements at 25 °C).

Sample MgO, Color	T_S /°C	Lattice Para-Meter a/pm	Occupation occ	Temperature Factor B_{eq}	Preferred [111] Orientation	Distances Mg-O/pm	Crystallite Size λ/nm
film light yellow	−190	424.63(8)	O 4b: 0.95 Mg 4a: 1.00	O: 0.1 Mg: 0.1		212	3
film white	25	423.48(2)	**Mg 8c: 0.10** **O 8c: 0.31** O 4b: 0.63 Mg 4a: 0.98	Mg: 1.3 O: 0.3 O: 0.2 Mg: 1.1	0.42	212 183	17
powder		421.184(1)	4b: 1.0 4a: 1.0	O: 0.1 Mg: 0.1		211	142
crystal [3]		421.47	4b: 1.0 4a: 1.0	O: 0.32 Mg: 0.35		211	

* *Fm*-3*m* (No. 225), Mg: 4a (0,0,0), O 4b (½,½,½) and 8c (¼,¼,¼).

To investigate this issue in more detail, we calculate the XRD difference maps, which are often used to verify or identify missing atoms in a structure model. The maps represent the difference between the electron density of a structure model (here, the model is anchored with Mg atoms in defined positions) and the experimental one obtained by 3D Fourier analysis [52,67]. Figure 3 shows these difference maps of the cubic cell occupied only by magnesium atoms (site 4a (0,0,0)) of the films deposited at 25 and −190 °C. The locations of the expected oxygen positions are displayed as clouds of increasing electron density, colored from red (low) over yellow to white (high). The map for the films deposited at −190 °C shows the expected positions for oxygen in the octahedral voids (site 4b (½,½,½)). However, the map for the films deposited at 25 °C reveals, in addition to the occupied octahedral voids, a distinct position for oxygen (or magnesium) in the tetrahedral voids (site 8c (¼,¼,¼)). In principle, both atoms, oxygen and magnesium, can occupy the tetrahedral voids of the rock salt structure. The Rietveld refinement, which considers the occupied tetrahedral voids, indicates that oxygen and magnesium are present at this site. The corresponding results are given in Table 1 and show partially filled octahedral and tetrahedral sites comprising magnesium and oxygen, together with larger temperature factors (B_{eq}) and crystallite sizes (λ = 17 nm), compared to the MgO films deposited at −190 °C (see also Figure S2 in Supplementary Materials). The refined occupation factors result in a formal overall composition of Mg:O of approximately 1.1:1.25 for the films deposited at T_S = 25 °C. Consequently, the occupation of both octahedral and tetrahedral sites formally corresponds to the formation of a superfilled rock salt structure. In detail, the octahedral sites of the rock salt structure are found to be partially filled with oxygen (occ: 0.63) but nearly full with magnesium (occ: 0.98). The tetrahedral site was found to be filled with 10% magnesium and 31% oxygen atoms. The overall excess of oxygen is somewhat unexpected, given that one would have expected an equal ratio of Mg:O = 1:1. Due to the largely identical electron density of Mg^{2+} and O^{2-}, it is difficult to distinguish between the two elements on the basis of the XRD data. Further analysis is clearly required to elucidate these deviations, as the Rietveld refinement does not allow a proper distinction between magnesium and oxygen atoms.

Usually, the superfilled rock salt structure describe above is not realized for ionic compounds such as oxides due to the presence of very short interatomic distances in this structure. Figure 4 depicts the superfilled rock salt structure next to the normal rock salt structure of MgO. For one of the oxygen atoms in the tetrahedral voids, the tetrahedral coordination by the surrounding magnesium and oxygen atoms is visualized. The occupation of the tetrahedral sites results in additional Mg-O distances of 183 pm (see Figure 4, black bonds). These distances are short but are a consequence of the occupation

of the fourfold coordination site inside the pre-defined rock salt structure with its usual sixfold coordination sites. These distances are quite plausible, since stable magnesium ketyl complexes, for example, exhibit Mg-O distances between 185 and 192 pm [68]. At the same time, short O-O distances of 183 pm (see Figure 4, red bond) are formed, which are much shorter than the O-O distances observed in MgO with 298 pm (in the rock salt structure), or the sum of the radii of two O^{2-} ions (264 pm [69]). However, dioxygen species such as superoxide and peroxide ions show O-O distances of 133 and 149 pm, respectively, which are shorter than the 183 pm observed in the superfilled rock salt structure.

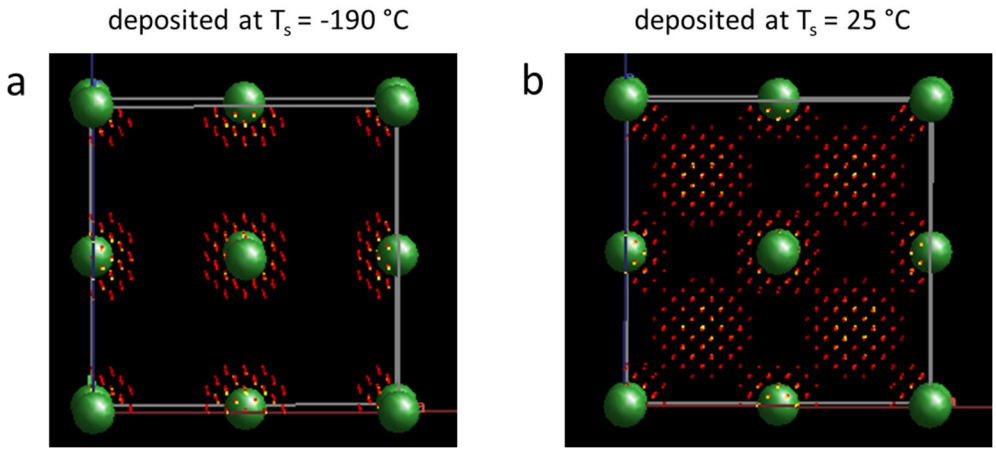

Figure 3. XRD difference maps of the MgO unit cell, including the Mg atoms (green spheres), of MgO films deposited at temperatures of −190 °C (**a**) and 25 °C (**b**). The color of the clouds changes (from red to yellow to white) with increasing electron density (from 1 to 6).

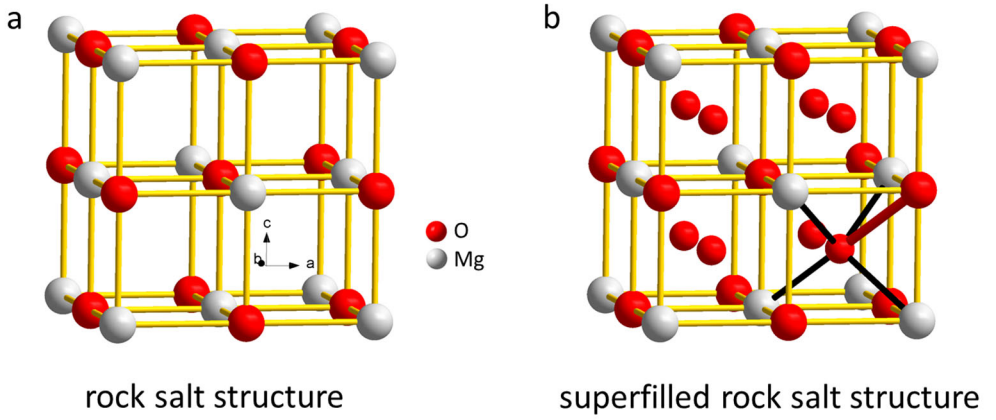

Figure 4. The MgO unit cell (Mg atoms gray and oxygen atoms red spheres) with Mg-O bonds (yellow line, viewing direction, see lattice parameters a,b,c) of the rock salt structure (**a**) and the superfilled rock salt structure with additionally occupied tetrahedral voids (**b**). The Mg-O distances of one of the oxygen atoms in the tetrahedral voids are visualized by the black bonds and one O-O distance by a red bond (both distances are 183 p.m.).

Thus, assuming that dioxygen species are also present in our films, these short O-O distances are feasible in magnesium oxide. In the case that magnesium atoms occupy the tetrahedral sites in the rock salt structure, extremely short Mg-Mg distances of 183 pm are formed. However, this is an unlikely occurrence, considering that the Mg-Mg distances in metallic magnesium are $d_{Mg\text{-}Mg}$ = 320 pm [70], in MgO $d_{Mg\text{-}Mg}$ = 298 pm [3], and in Mg(I) compounds around $d_{Mg\text{-}Mg}$ = 285 pm [71], respectively, which are considerably larger than the 183 pm Mg-Mg distance that appears when placing Mg atoms in tetrahedral sites of the MgO rock salt structure. Thus, trying to accommodate the occupation of tetrahedral

sites by Mg atoms would imply the existence of rather large local distortions of the rock salt structure.

3.3. Raman Spectroscopy

Raman measurements were performed to gain deeper insight into the local ordering of the deposited MgO films. Figure 5 presents the Raman spectra for the films deposited at −190 °C and at 25 °C, together with the spectrum recorded on a MgO single crystal. All spectra in Figure 5 were recorded at −190 °C because these Raman measurements provide more distinct bands.

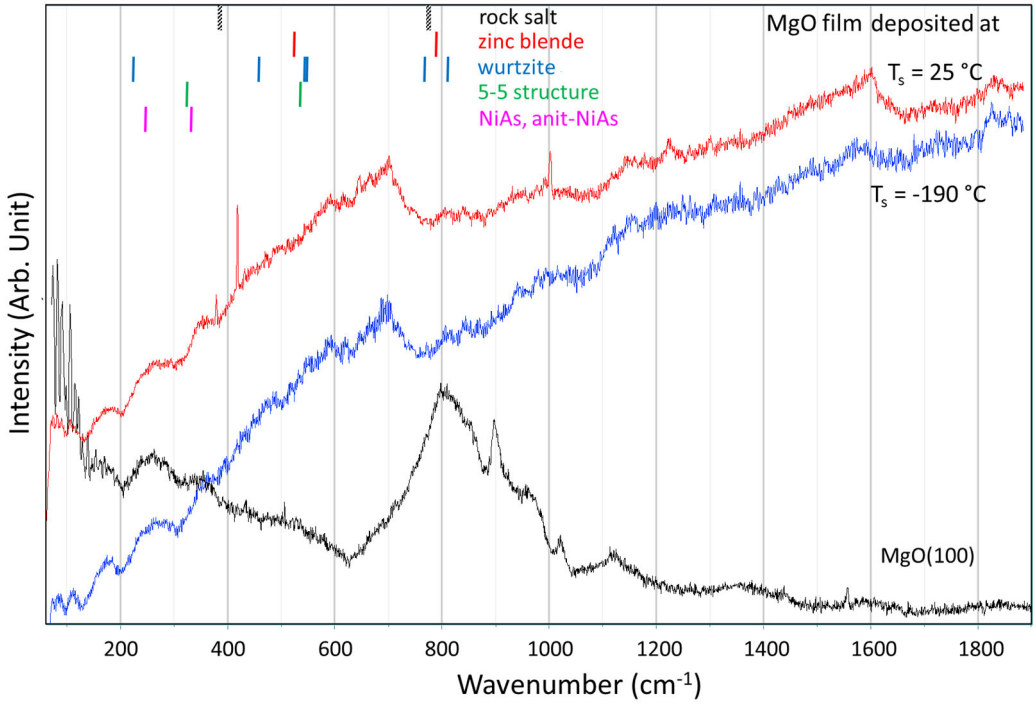

Figure 5. Raman spectra of MgO films deposited at temperatures of 25 °C (red curve) and −190 °C (blue curve), together with the Raman spectrum of a MgO(100) single crystal (black curve). The spectra are vertically shifted for better visualization. All measurements were performed at −190 °C. The calculated wavenumbers of the rock salt and different hypothetical structures of MgO (B3LYP method) are shown in the upper part as colored lines (see text).

Theoretical calculations using the DFT method give results for the vibrational spectrum of MgO, with a transverse and longitudinal optical mode at 414 cm^{-1} (TO) and 710 cm^{-1} (LO), respectively (at the center of the Brillouin zone) [72]. In general, these first-order Raman bands are not visible for MgO due to the inversion symmetry of the rock salt structure. Nevertheless, first-order Raman modes have been reported for MgO nanomaterials, but most of the observed and assigned wavenumbers originate from impurities and do not belong to MgO [73]. Thus, only second-order bands of MgO have been unambiguously detected, occurring between 500 and 1500 cm^{-1} [74]. These observed wavenumbers are in good agreement with our measurements on purchased MgO single crystals. However, we detect additional sharp bands around 100 cm^{-1} and at 1556 cm^{-1} in addition to broad bands between 200 and 600 cm^{-1} for the single crystalline MgO. The sharp band at 1556 cm^{-1} can be assigned to O_2 molecules, which show the symmetric stretching mode at 1552 cm^{-1} [75]. Thus, it seems that O_2 molecules are embedded in the crystals during the growth process. All the other new bands we observe for the single-crystal of MgO can be explained by the effects of disorder inside the MgO crystal resulting from the incorporation of oxygen molecules (see below for more details).

In contrast, the Raman spectra of our MgO films (see Figure 5) do not exhibit these distinct second-order Raman bands of MgO crystals (600 to 1200 cm^{-1}). For all obtained

films (deposited at 25 °C, and −190 °C, respectively), very broad Raman bands are present in the entire measured range from 70 to 1900 cm^{-1}. This result supports a very high disorder in the films; we note that especially the range between 800 and 1900 cm^{-1} differs from the spectrum of the MgO crystal. In that range, broad bands around 1000, 1200, 1600 and 1800 cm^{-1} were detected. This region is dominated by the O-O stretching vibrations of various dioxygen species such as O_2^{2-} (840 cm^{-1}), O_2^- (1150 cm^{-1}), and O_2 (1552 cm^{-1}) [52], and suggests the existence of such species also in our MgO films deposited at 25 and −190 °C. The O-O stretching mode of the peroxide ion in bulk MgO_2 is observed at 864 cm^{-1} and a weaker one at 934 cm^{-1} [76]. Under high pressure, the stretching mode of MgO_2 increases from 857 cm^{-1} (1 bar) to 1037 cm^{-1} at 104 GPa [77]. Thus, the broad bands in our films between 800 and 1100 cm^{-1} may be due to incorporated peroxide ions, which are exposed to high local effective pressures due to the surrounding lattice.

Considering that MgO crystals also contain O_2 molecules, the presence of embedded O_2 and other dioxygen species such as superoxide ions (O_2^-) in our films seems distinctly possible. This incorporation leads to very broad Raman bands in the range of 1200 to 1800 cm^{-1}, mainly caused by different O-O distances formed. This also creates a displacement of the surrounding atoms, which is associated with different Mg-O distances. The different Mg-O distances are then reflected by the Raman bands in the range between 70 and 700 cm^{-1}, which are most pronounced between 300 and 700 cm^{-1}. It is noticeable that the columnar MgO films deposited at 25 °C show not only a more structured spectrum but also three additional sharp Raman bands at 378, 418 and 1002 cm^{-1} compared to the spectrum of the films deposited at −190 °C. Typically, sharp Raman bands are associated with ordered structures (cf. [78]); thus, the three sharp bands indicate highly ordered regions/particles within the MgO films and can be related to the superfilled rock salt structure. The bands at 1002 cm^{-1} fit well with the O-O stretching mode of peroxide ions but the assignment of the other two sharp bands is more difficult. Therefore, we have calculated the Raman bands of MgO crystallizing in different (hypothetical) structures, which are further discussed in the Discussion section.

3.4. EDX and XPS Spectroscopy

The composition of the films is an important issue with respect to the observed structural features. Therefore, the composition was also determined by EDX and XPS analysis and the results are shown in Table 2. The EDX data, obtained from a film depth of up to 1.5 µm, show a stoichiometric MgO in the films deposited at 25 °C and a high oxygen excess of about 50% for the films deposited at −190 °C. The EDX analysis at different voltages shows that there are no significant variations in the Mg:O ratio at depths between about 150 nm and 1.5 µm. The compositions extracted from the XPS data of the as-received films, which originate from the surface (1–5 nm depth), show the same trend, but with an oxygen deficit of about 30% for the film deposited at 25 °C and a near stoichiometric ratio for the films deposited at −190 °C. Subsequently, the film surfaces were sputtered (10 min with Ar^+ ions) and the XPS spectra were re-measured, showing a reduced oxygen content for both films (T_S = −190 °C: −31%; T_S = 25 °C: −13%). This fact implies a higher loss of oxygen during the sputtering process compared to magnesium and suggests, at least partially, rather weakly bound oxygen atoms in the surface or grain boundary regions of the original films. Thus, the films deposited at −190 °C, which consist of solid, compact pieces, contain a high excess of oxygen inside the films, which is then reduced at the surface. The columnar films deposited at 25 °C are stoichiometric with an excess of Mg on the surface. Comparison with EDX and XPS data obtained from single crystal MgO supports the oxygen excess for the films deposited at −190 °C and stoichiometric MgO films deposited at 25 °C. The oxygen loss due to the sputtering process is also detected (−11%), which is similar to the loss of the MgO films deposited at 25 °C. In general, the comparison with the MgO crystal shows that the compositions obtained from XPS measurements seem to underestimate the oxygen content in MgO samples.

Table 2. Composition of MgO films analyzed by EDX and XPS measurements compared to a MgO(100) single crystal.

MgO Sample	EDX Film	XPS Surface	XPS After Sputtering
film T_S = 25 °C	MgO = 1:0.99	MgO = 1:0.73	MgO = 1:0.63
film T_S = −190 °C	MgO = 1:1.50	MgO = 1:1.06	MgO = 1:0.73
crystal (100)	MgO = 1:1.00	MgO = 1:0.79	MgO = 1:0.70

In addition, the XPS measurements also provide oxygen and magnesium binding energies of the core levels. The XPS spectra of O 1s in Figure 6 show the presence of two oxygen peaks in both films. The lower binding energy peak at 529.6 eV is attributed to the O^{2-} lattice oxygen in MgO. This is in agreement with the spectrum recorded on a single crystal MgO(100) sample (O 1s: 529.4 eV) [79]. The higher binding energy peak of the O 1s spectra in Figure 6 at ca. 532 eV is due to the presence of less reduced oxygen (compared to O^{2-}), probably in the form of dioxygen species such as peroxide ions (cf. [14]), which are more abundant in the films deposited at −190 °C. After sputtering of the film surfaces, the intensity of the high-energy peaks decreases to about one-third of the previous value for all films. The existence of MgO_2 species on the surface has previously been described for MgO films grown at about room temperature [80]. In these films, a similarly high binding energy for the peroxide ions is found in the O 1s spectra. However, the high content of the less reduced oxygen species in our films, both on the surface and inside, is quite extreme. In particular, the films deposited at −190 °C contain a higher content of less reduced oxygen near the surface compared to the lattice oxygen atoms. In the literature, the same high binding energies of O 1s are often associated with the formation of hydroxide at the surface of MgO films [81]. However, the presence of hydroxide species in our films is excluded because all samples are handled completely under vacuum or in an Ar atmosphere, from the deposition process to the various measurements with analytical tools. Therefore, the high content of less reduced oxygen in our samples cannot be due to hydroxides. For comparison, the O 1s core levels of the single-crystal MgO were also measured (see Figure 6). Surprisingly, the XPS spectra show three oxygen peaks at 529.5, 531.5, and 533.5 eV. The first two (529.5, 531.5 eV) correspond to the oxygen core levels of oxide and peroxide ions as described for the MgO films. However, the third one at 533.5 eV was not detected in the films and is consistent with O 1s peaks of adsorbed O_2 molecules. The O 1s peak of adsorbed molecular oxygen on a Ni(100) surface at −193 °C has been observed at 534 eV [82]. All O 1s peaks are still present after sputtering with almost the same ratio. This result strongly confirms the presence of embedded O_2 in our purchased MgO crystals in addition to oxide and peroxide ions. All these species are present throughout the crystal and their ratio is not affected by the sputtering process. This is different in our films, where the heights of the less reduced oxygen peaks (peroxide ions) are greatly reduced by the sputtering of the surface, suggesting weakly bonded dioxygen species in the MgO films. In addition, the Mg 1s and 2p core-level spectra of the MgO films were also measured (Figures S3 and S4 in Supplementary Materials). These spectra show an asymmetric Mg peak shape, which also supports the presence of different oxygen species surrounding the magnesium atoms. Furthermore, metallic magnesium could not be identified from the measured Auger KLL peaks of the MgO films (Figure S5 in Supplementary Materials).

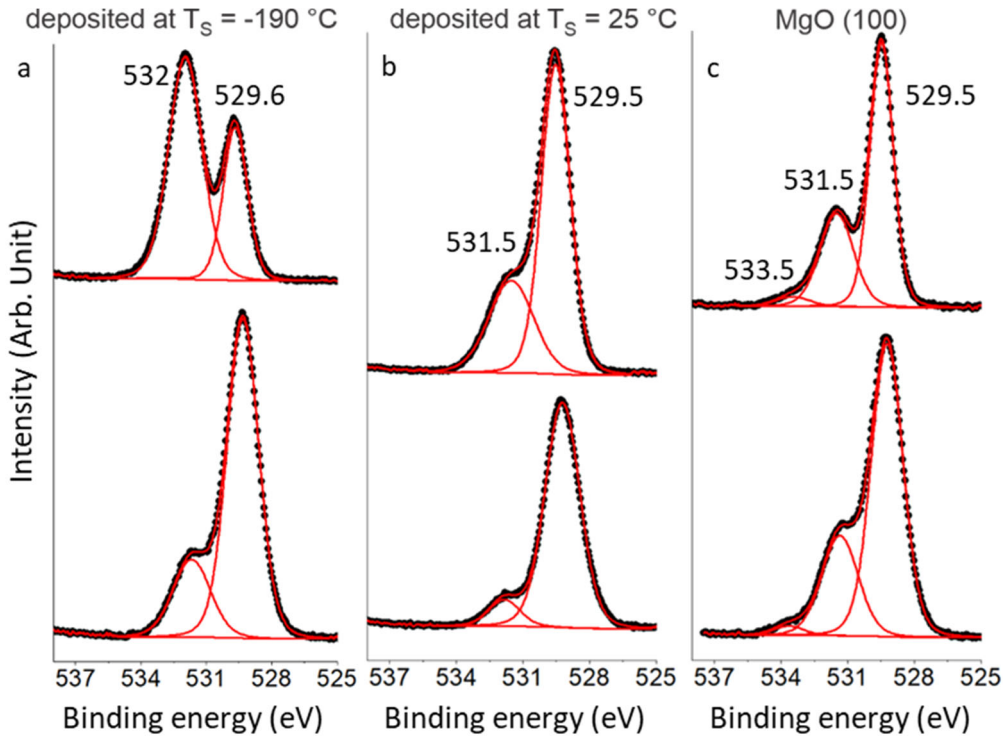

Figure 6. O 1s XPS spectra of MgO films deposited at −190 °C (**a**) and 25 °C (**b**) compared to a MgO(100) single crystal (**c**); top as deposited, and bottom after sputtering with Ar^+ ions for 10 min.

4. Discussion

As we have seen in the description of the results in the preceding section, two completely different MgO films are formed just by changing the substrate temperature T_S of the deposition. This refers not only to the stark difference in the morphology of the films but also to their atomic structures. At a substrate temperature of −190 °C, compact, light-yellow films with a high excess of oxygen are obtained, which contain very small crystallites of the rock salt structure. In contrast, deposition at a substrate temperature of 25 °C forms nearly stoichiometric, white, columnar films consisting of a superfilled rock salt structure.

4.1. Synthesis Process

What is special about the deposition process used to achieve this unusual result? First, the deposition is performed at low substrate temperatures, i.e., room temperature and below. Second, we use very high deposition rates (ca. 1 monolayer per second), which means that all incoming species are immediately covered and thus do not have much opportunity to diffuse on the surface to establish an ideal global minimum single-crystal-like structure, which is a hit-and-stick process. Third, we use a 10-fold excess of plasma-activated oxygen. And fourth, the difference results from the mobility of the surface species (atoms, molecules, etc.), which is controlled by the substrate temperature. Thus, the high oxygen contents detected in the samples are caused by the synthesis parameters used and are realized in the samples in two different ways. At T_S = −190 °C, the deposition conditions lead to the incorporation of excess oxygen at grain boundaries, and at T_S = 25 °C, as interstitial oxygen within the rock salt structure, respectively. This finding suggests the following scenario. The higher mobility of the adsorbed species on the substrates at room temperature leads to local rearrangements that allow the insertion of oxygen species into the rock salt structure, accompanied by the formation of larger crystallites. On the other hand, the low temperature (T_S = −190 °C) is associated with a reduced mobility on the surface and, thus, the high excess of oxygen species sticking on the surface of small nanosize crystallites are incorporated between the grains of the film, preventing the growth of larger crystallites.

The cracked pieces and the flat hills (unburst bubbles) formed on the surfaces of the films deposited at −190 °C seem to be caused by escaping/rising oxygen-containing bubbles during the deposition process and, possibly, also during the warming up of the samples to room temperature. These observations, together with the large loss of oxygen (mainly dioxygen species) during sputtering in the XPS chamber, support the presence of weakly bonded oxygen at the grain boundaries that can easily leave the samples. Furthermore, all samples exhibit a reduced oxygen content in the near-surface region, as evidenced by XPS analysis. This reduction is attributed to the presence of distinct dioxygen species incorporated into the films deposited at −190 and 25 °C, respectively.

We note that the size of the crystallites is in the nanometer range and increases with the substrate temperature. Thus, the outcome lies between the achievable limits of highly oriented films with large crystalline regions generated, e.g., via MBE [18] on the one extreme, and the essentially amorphous films obtained, e.g., by sputtering [30] on the other one.

4.2. Dioxygen Species at Grain Boundaries

The structural arrangement of the embedded oxygen species at the grain boundaries in the MgO films for T_S = −190 °C is not very clear. One problem is that only the ordered domains are visible in the X-ray powder pattern. The fact that the oxygen is easily released suggests weakly bonded or adsorbed O_2 dimers between the MgO crystallites, in contrast to the oxygen incorporated in the superfilled rock salt structure. In this context, we note that studies of ZnO films reveal that the yellow color of ZnO is caused by the presence of superoxide ions in the material [53]. This suggests that the light-yellow color of MgO films deposited at −190 °C may also be caused by the presence of superoxide ions. Due to the flexibility of the interfaces associated with the grain boundaries, O_2 dimers and charged dioxygen species, such as superoxide ions, can exist at the grain boundaries, in principle. Figure 7 shows a small rock salt crystallite of MgO with a surrounding shell of oxygen atoms. For better visualization, a 2D flat 5 × 5 supercell (1 unit cell thick) is drawn forming a particle with a diameter of about 3 nm. The shell is constructed by saturating all terminal Mg atoms with oxygen atoms. The complete 3D MgO crystallite (5 × 5 × 5 supercell) contains 1694 magnesium and oxygen atoms embedded in an oxygen shell of 450 atoms. This results in a composition of $MgO_{1.53}$ (Mg:O = 1:1.53), which is consistent with the composition determined by EDX measurements. These particles can form grain boundaries by connecting these crystallites through the oxygen atoms of the shell, as shown in Figure 7. The O-O dimers formed in this fashion are shown for the flat 5 × 5 supercell, where on one side a connected crystallite is partly shown (for better distinction all oxygen atoms of the surrounding crystallites are drawn in purple). The O-O bonds formed are very flexible and can be easily adapted to the O-O distances of different dioxygen species (149 pm for peroxide, 133 pm for superoxide ions, 121 pm for oxygen dimers).

The very small size of the nano-size crystallites in the film results from the presence of a high density of nuclei of crystallization combined with the low mobility of the MgO species under the deposition conditions employed, which prevents the coarsening of the size distribution of the crystallites that usually eliminates small crystallites in favor of larger ones, analogous to the Ostwald ripening process. Furthermore, we note that the O-O distances of the dioxygen species embedded in the grain boundaries separating the crystallites are very flexible.

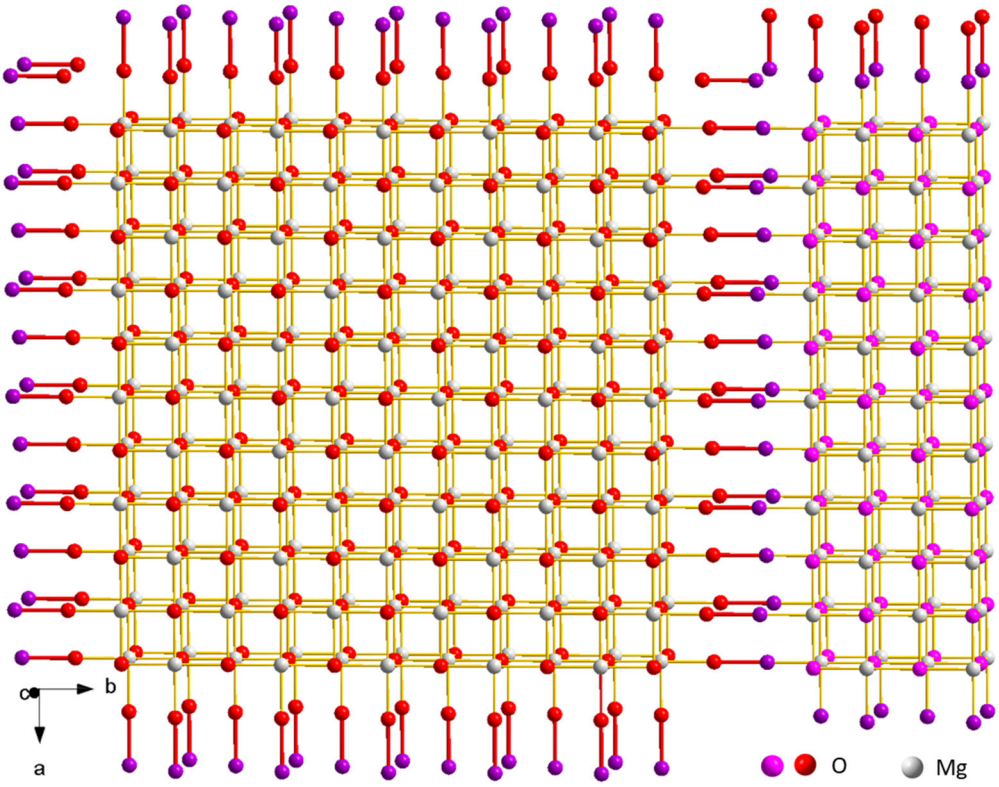

Figure 7. Dioxygen species embedded at grain boundaries. Connection of MgO crystallites which form the rock salt structure: 5 × 5 × 1 supercell (diameter ca. 3 nm) with a surrounding shell of oxygen atoms formed by saturation of all terminal Mg atoms with oxygen atoms (oxygen atoms drawn in red, Mg-O bonds: yellow lines). The grain boundaries are visualized by the connection of the oxygen atoms of the shells. A partially connected crystallite is shown on one side (all oxygen atoms of the connected crystallites are drawn in purple, the O-O bonds formed are shown as red lines).

4.3. Superfilled Rock Salt Structure

In the MgO films deposited at room temperature, the excess oxygen is responsible for the filling of some of the interstitial tetrahedral voids of the rock salt structure. Thus, approximately 40% of the tetrahedral voids are occupied, as shown by the Rietveld refinement. This is a superfilled rock salt structure with a high atomic density. How can this unusual arrangement, which is not normally achievable in ionic compounds, be stabilized? We begin by examining the oxygen atoms, which are the predominant occupants of the tetrahedral sites. On the one hand, the interstitial oxygen atoms form four O-O distances (183 pm), which are larger than the interatomic distances of known dioxygen species, such as peroxides (149 pm) and superoxides (133 pm) ions. At the same time, four Mg-O distances (183 pm) are formed, which are shorter than the Mg-O distances of tetrahedrally coordinated magnesium in ternary compounds, which are between 190 and 198 pm [83]. Thus, the observed unusual arrangement can be interpreted as a compromise between these two requirements. There is no evidence in the refinements for local larger displacements compensating the distance differences or for disordered O_2 dumbbells, e.g., by unusually large temperature factors for the Mg atom positions. Furthermore, the situation for MgO is different from an analogous irregular filling of voids in ZnO, where the flexibility of the wurtzite structure (the lattice parameter c can be adjusted against the parameter a) tolerates filling both face-connected Zn tetrahedra by oxygen atoms, and thus the resulting superoxide ions fit easily into the structure [52]. In contrast, magnesium oxide in the rock salt structure lacks this possibility (only one free lattice parameter a). Another very important aspect is the fact that the coordination number of the oxygen atoms surrounding the magnesium atoms increases drastically from 6 to 14 (=8 + 6) by occupying the tetrahedral sites.

A solution to avoid this high coordination number of Mg is a segmentation of the superfilled rock salt structure into two connected parts, one with oxygen on tetrahedral sites and another with oxygen on octahedral sites. This scenario is illustrated in Figure 8. The superfilled rock salt structure is divided into interconnected rock salt and zinc blende parts with a continuous Mg fcc-type sublattice. Both structures have a 1:1 composition, with sixfold (212 pm) and fourfold (183 pm) coordination of magnesium through oxygen and vice versa for the rock salt and zinc blende structures, respectively. In the zinc blende structure one half of the available tetrahedral sites are occupied. Since the oxygen atoms occupy one third of the tetrahedral sites (8c: occ = 0.31), which corresponds numerically to the occupied oxygen atoms on the octahedral sites (4b: occ = 0.63), it follows that the zinc blende structure and the rock salt structure are present in the sample in equal portions. In addition, the octahedral and tetrahedral sites are not completely occupied by oxygen atoms. The presence of magnesium in tetrahedral voids can be described as an inverted lattice, where the oxygen provides the fcc packing and the magnesium atoms occupy the corresponding voids. This inverse structural arrangement is readily achievable due to the interchangeability of the respective sublattices in both structures. The splitting compensates for the dense atomic packing. Particularly noteworthy is the transition region between the two structures. In the transition regions, there will be a decrease in the coordination for magnesium atoms by oxygen atoms from 6 to 5 and finally 4, which is compensated by the shorter tetrahedral Mg-O distances; in a simple electrostatic model picture, this would increase the Mg-O Coulomb interaction for each Mg-O pair in a favorable way. The coordination of the magnesium atoms by oxygen atoms in the zinc blende structure (4× 183 pm) can also be extended by adding further oxygen atoms with Mg-O distances of 212 pm. This is in agreement with the present DFT calculations, where the zinc blende structure in MgO is computed (4× 196 pm HF, 4× 197 pm B3LYP, and 4× 196 pm PBE, see Supplementary Materials), while the wurtzite and the 5–5 structures have calculated Mg-O distances smaller than 200 pm. On the other hand, present ab initio calculations concur with experimental Mg-O distances in the rock salt structure (6× 209–212 pm, see Table 1 and calculated crystal structure data in Supplementary Materials), while other predicted 6-fold coordinated MgO structures in the NiAs and anti-NiAs type are computed to have Mg-O distances in the range 210–213 pm. In addition, there are some short O-O distances in the transition region between the oxygen atoms in the tetrahedral and octahedral sites. The same occurs in the transition region for the Mg atoms occupying the tetrahedral and octahedral sites. Here, very short Mg-Mg distances of 183 pm are formed. However, these very short Mg-Mg distances can be avoided by the insufficient occupancy of sites (tetrahedral and octahedral), and thus the occupancy of magnesium in the tetrahedral site is also feasible. This structural arrangement helps to understand the superfilled rock salt structure, which can be stabilized by the locally separated filling of the oxygen sites, thus forming both rock salt and the zinc blende type structured segments.

In summary, in this superfilled rock salt structure, a face-centered cubic Mg sublattice is present with filled tetrahedral and octahedral voids in separate segments. This segment-based arrangement prevents the formation of an overly large number of short (O-O/Mg-Mg) contacts within the superfilled rock salt structure, which would appear if too many neighboring octahedral and tetrahedral voids were occupied. Moreover, the short O-O distances present in the transition regions between the two segments can be easily accounted for by the formation of dioxygen species. The short Mg-Mg distances that can appear in the transition regions can be avoided by the presence of vacancies in the Mg sublattice resulting in an oxygen environment around the magnesium atoms on tetrahedral sites.

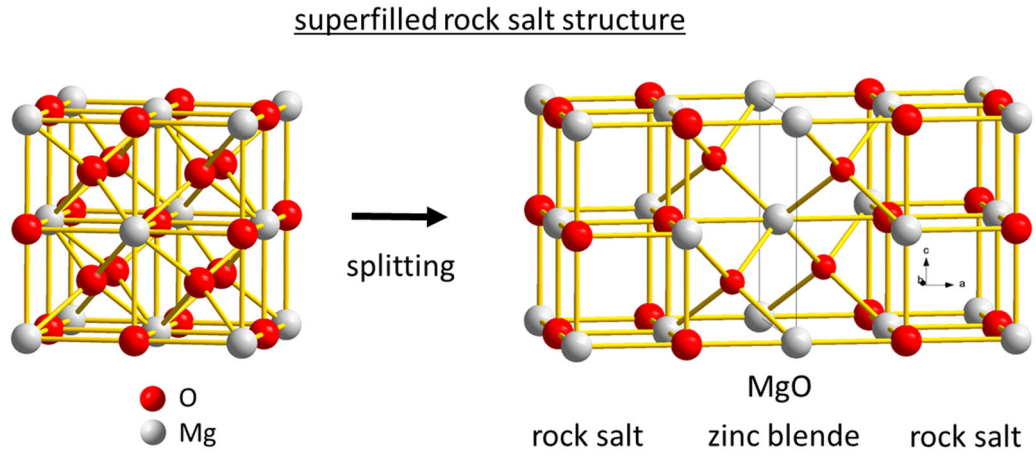

Figure 8. The superfilled rock salt structure of MgO consists of a Mg fcc-type sublattice with oxygen atoms in octahedral and tetrahedral voids. The splitting into connected segments, where either the octahedral sites are filled, forming the rock salt structure, or the tetrahedral sites are half-filled, forming the zinc blende structure, while maintaining the same Mg sublattice, stabilizes this structure (viewing direction, see lattice parameters a,b,c). In addition, the octahedral and tetrahedral sites are not fully occupied.

4.4. Raman Analysis

The structural characteristics of the MgO films are also reflected in the Raman spectra. For example, the O-O distances of the dioxygen species, which are suggested for films deposited at −190 °C to be located in the shell and at 25 °C in the superfilled rock salt structure, respectively, can be associated with the broad bands in the range between 800 and 1900 cm^{-1} in all Raman spectra of the films. For the films deposited at −190 °C, the dioxygen species are located between the crystallites at the grain boundaries, allowing flexible adjustment of the O-O distances. For the films obtained at 25 °C, which form the superfilled rock salt structure, the O-O distances are more rigidly restricted by the surrounding lattice. In all cases, the dioxygen species are more or less confined by surrounding atoms. We recall that the specific wavenumbers in a Raman spectrum are determined by the effective force constants between the atomic species. This force depends not only on the distances between the neighboring atoms but also on the surrounding rigid lattice. Calculations of the Raman vibrations for dioxygen species in ZnO show a shift to higher wavenumbers for embedded dioxygen species [53]. Thus, for the Raman bands of our films, the range derived for predominantly free dioxygen ions (840 to 1552 cm^{-1}) can be extended to wavenumbers up to 1900 cm^{-1}. This also implies that the real O-O distances can be longer than the ones expected from the specified wavenumbers. In addition to the O-O vibrations, the Mg-O dominated vibrations should also be reflected in the Raman spectra. The expected first-order bands of the Mg-O lattice appear between 300 and 800 cm^{-1}, but due to the structural symmetry of the crystals these bands are only visible for the proposed zinc blende arrangement and not for the rock salt structure. Disordering phenomena can bypass this strong rule and thus the broad bands between 300 and 800 cm^{-1} are assigned to Mg-O vibrations of a partly disordered lattice. However, only the vibration of the zinc blende structure or other structures (that do not exhibit inversion symmetry) can lead to sharp bands. To clarify this, we calculated Raman bands of different (hypothetical) structures and compared them with our measurements. Table S1 (Supplementary Materials) presents the calculated Raman wavenumbers of MgO forming rock salt, zinc blende, wurtzite, NiAs, anti-NiAs, and the 5–5-type structure. The wavenumbers of these structures calculated using the B3LYP method are also displayed as colored lines in the upper part of Figure 5.

The calculated wavenumbers of all these structures can be divided into two sets. One group is located at around 800 cm^{-1} and the second one between 200 and 600 cm^{-1}, respectively. Both more or less match the two modes of the rock salt structure at 387 cm^{-1} (TO) and at 770 cm^{-1} (LO), respectively. However, there is no satisfactory match between

these calculated wavenumbers and our observed sharp Raman bands at 378 and 418 cm^{-1} of the films deposited at 25 °C. Thus, the structural arrangement of these highly ordered regions in the films, which are responsible for these wavenumbers, is therefore different from all the crystal structures used for calculations. This means that the structural variability in our sample is particularly restricted and is not represented by the our calculated MgO structures. In addition, we have calculated the wavenumbers of MgO_2, which crystallizes in the pyrite structure. The calculated wavenumbers are between 400 and 500 cm^{-1} next to the O-O mode of the peroxide ion between 830 and 1092 cm^{-1} (cf. calculated crystal structure data in Supplementary Materials). This result confirms the observed sharp wavenumber at 1002 cm^{-1} as an O-O stretching mode, but does not allow a clear assignment of the other two sharp wavenumbers of the Raman spectra of MgO films obtained at 25 °C.

The structural disorder we consider for the MgO films can, in principle, also exist in a modified form in MgO crystals. The detection of noticeable amounts of O_2 molecules and peroxide ions inside the MgO crystals (Raman, XPS) indicates that a certain amount of disorder must be present, which then also influences the Mg-O distances. Since the first-order Raman bands are not observed, the measured Raman intensities of MgO are generally low. Thus, the observed Raman bands are usually attributed to second-order scattering, which, practically by definition, will be of rather low intensity. However, it is also possible that these bands originate from the disorder present in the MgO crystals. Furthermore, the relatively sharp bands at 897 and 1021 cm^{-1} can be assigned to peroxide ions, the one at 1557 cm^{-1} to the O_2 dimer, and the broader band at 1113 cm^{-1} to superoxide ions, respectively. Similarly, the high-intensity broad band at about 800 cm^{-1} should belong to the LO mode, and the one between 200 and 400 cm^{-1} to the TO mode of MgO, respectively. The latter modes are only weakly visible due to disorder. In addition, many sharp bands are observed in the region around 100 cm^{-1}, which is dominated by Mg-Mg vibrations. Thus, all the bands in the Raman spectrum of single-crystal MgO can be attributed to the corresponding disorder caused by the embedded O_2 molecules, without needing to consider any second-order excitations.

4.5. Dioxygen Species and Charge Balance

The formation of peroxide ions in the MgO system is not new. First of all, magnesium peroxide MgO_2 exists as a bulk material (e.g., precipitation from a solution of H_2O_2) crystallizing in the cubic pyrite structure with a lattice constant a = 484.41 pm [84], which is in good agreement with our GGA-PBE, B3LYP and Hartree–Fock calculations (483.1 to 490.4 pm, see Supplementary Materials). In principle, this is 15% higher than the lattice constant of MgO (rock salt structure). MgO and oxygen also react at approx. 1880 °C and 96 GPa to form MgO_2 [77]. Electron microscopy studies show the formation of crystalline MgO_2 thin films on the surface of MgO crystals after heating the samples to about 1200 °C under high vacuum [85]. XPS measurements also support the presence of MgO_2 on the surface of MgO films deposited at room temperature [80]. Furthermore, the analysis of the growth process [38] reveals that the singlet oxygen atoms strongly bind to the surface oxygen, forming stable peroxide ions, while oxygen atoms in the metastable triplet state can diffuse on the surface over a wide temperature range. In contrast, the molecular oxygen is very loosely bonded to the surface and can only be incorporated by reacting with defects such as O vacancies. Thus, these studies support the presence of dioxygen species (peroxide ions, etc.) and also the insertion of oxygen in our films, especially when deposited at −190 °C. The formation of peroxide ions is accompanied by a reduced anion charge ($2O^{2-} \rightarrow {O_2}^{2-} + 2e^-$) compared to the oxide ions, which compensate the higher oxygen content.

For T_S = 25 °C, the Rietveld refinements of the films show an excess of oxygen for the superfilled rock salt structure. Due to the largely identical electron density of Mg^{2+} and O^{2-}, the composition determined by the Rietveld method of the superfilled rock salt structure is prone to error. Conversely, the EDX and XPS analyses provide more reliable values, with a composition that is nearly stoichiometric for these films deposited at 25 °C. Nevertheless,

the local formation of dioxygen species is supported by the structural segmentation as discussed above. Thus, a local charge imbalance seems possible, even if the specific realization remains unclear. In principle, a negative charge excess can also be compensated by reducing the oxidation state of the magnesium atoms from Mg^{2+} to Mg^{+} or even Mg^{0}. An indication of this seems to be the formation of a black MgO film, which we obtained in one experiment at room temperature. The black color can be caused by mixed-valent magnesium ions, in analogy to the nonstoichiometric transition metal oxides. Furthermore, the d^0 ferromagnetism of MgO films can be triggered by this circumstance. Black MgO films have also been obtained on cooled shielding plates by ballistic deposition of MgO using an electron beam evaporator [86]. The occurrence of black films is explained by an oxygen-deficient MgO matrix containing metallic magnesium. However, our columnar black MgO film shows no signals of metallic magnesium in the XPS spectrum (Auger KLL) and is stoichiometric.

The charge balance situation is different for the films deposited at −190 °C, where the EDX data give a ratio of Mg:O = 1:1.5. In this case, the charge is balanced when the excess oxygen atoms form neutral O_2 dimers at the grain boundaries. However, these species experience almost no attractive bonding to the crystallites. For a weak bond formation of these dioxygen species at the grain boundaries, charge transfer from the oxide ions of the crystallites to the dioxygen species can occur. This should lead to an expansion of the Mg-O distances (next to the O-O distances of the shell), followed by an increase in the lattice constant, which is observed for our films (cf. Table 1). The Raman results also support the formation of different dioxygen species in these films by the many bands observed in the region of the O-O stretching vibrations.

4.6. Surface Species and Bond Formation

The analysis of the MgO growth process reveals that magnesium atoms readily evaporate from substrates at room temperature [87] and must be captured by oxygen to form MgO [88]. Thus, a critical oxygen flux is required to initiate the growth process. Furthermore, the known low diffusivity of MgO molecules leads to the formation of defects at room temperature [41], and the incorporation of oxygen atoms, that are not fully coordinated by magnesium, occurs at substrate temperatures of about 500 °C [37]. This means that the components (Mg, O, O_2) are very volatile while the formed MgO species are rather immobile. One reason for this could be the large enthalpy of formation of MgO which is reflected by a high Mg-O bond energy and a very low enthalpy of MgO at standard conditions. The formation enthalpy of MgO per atom is 300.6 kJ, which is at the same high level as the released enthalpy for the formation of Al_2O_3 (corundum, 335 kJ per atom [2]). This highly exothermic reaction is used, for example, in the Goldschmidt process for joining railroad tracks by iron welding. Therefore, for the formation of Mg-O species on a substrate, another molecule or atom (collision partner) is required to conserve the energy and momentum, otherwise the Mg-O can easily re-evaporate again. In this context, we note that in contrast to the gas phase, the surface can take up excess momentum and energy associated with the reaction. However, as simulations have shown [89], this loss of energy usually cannot take place instantaneously, i.e., several collisions are required to do so with a partial loss of energy and momentum at each bounce, and thus the atoms and molecules experience several bounces on the surface until they are fully adsorbed on the surface and can form bonds with each other and the surface atoms. The observed dependence of MgO deposition rates on oxygen pressure (onset at low pressure and decrease at high pressure [34]) can also be attributed to this effect. Only in a limited intermediate range can the released bond energy be distributed and MgO film growth start. At lower and higher pressures, the formed Mg-O species desorb again. This goes hand in hand with high deposition rates, which involve enough collisions that are necessary for the growth of MgO using the elements, magnesium and oxygen. In our experiments with an oxygen pressure of 2.5×10^{-5} mbar, no MgO deposition is optically visible at Mg source temperatures below 370 °C. Furthermore, the

high enthalpy of formation is responsible for the low effective mobility of the formed MgO species, once the energy released has been absorbed by the substrate.

4.7. Structure Nomenclature

Finally, a note about our terminology 'superfilled rock salt structure'. An fcc packing of atoms with all tetrahedral and octahedral voids filled is described in the literature as the Cu_2MnAl structure type (ICSD, inorganic crystal structure database) or as the BiF_3 type (ICDD, international center for diffraction data), and sometimes also as the Li_3Bi type. This structure type is common in alloy systems, but not in ionic compounds. Only metalloid rare earth hydrides [90], lithium nitride [91], and sodium nitride [92] under very high pressure crystallize in this structure. According to recent results, even BiF_3 does not form this crystal structure [93]. Thus, there appears to be no purely ionic compound that forms this structure under standard conditions, and therefore we feel that it does not make much sense for us to refer to alloy compounds. Furthermore, the tetrahedral and octahedral sites in the fcc packing of the Mg atoms in the MgO films obtained here are only partly occupied in our superfilled rock salt structure. Therefore, the labeling of the structure in our films as a superfilled rock salt structure is more suitable than to talk about a partially filled Cu_2MnAl type structure. Furthermore, this terminology also more clearly maintains the relationship to the standard rock salt structure of MgO.

5. Conclusions

While both magnesium oxide and peroxide are known as bulk materials, the formation of MgO_2 in films has only been observed on the surface of MgO films. In the present study, the deposition of magnesium together with activated oxygen in the ballistic deposition region allows the incorporation of dioxygen species (O_2^{2-}, O_2^{-}, O_2, etc.) located at grain boundaries, and as interstitial oxygen filling tetrahedral sites in the MgO rock salt structure. However, the details of the deposition process influence not only the film morphology but also result in very different atomic structures of the MgO films.

The combination of high deposition rates and very low substrate temperatures ($T_S = -190$ °C) leads to embedded dioxygen species in the grain boundaries of nanometer sized (rock salt-type) crystallites of the polycrystalline MgO films. Since the dioxygen species mainly reside in the grain boundaries separating the crystallites, their O-O distances are very flexible.

In contrast, films prepared via high deposition rates at room temperature result in a superfilled rock salt structure, where a face-centered cubic Mg sublattice is present with filled tetrahedral and octahedral voids in separate segments. In the transition regions between the two segments, there are short O-O distances that can easily be attributed to dioxygen species. Due to the rather rigid Mg atom lattice, the range of feasible O-O distances in the case of the superfilled rock salt structure is much more limited than for the dioxygen species located in grain boundaries.

This is the first instance in which the presence of dioxygen species, including peroxide and superoxide ions, has been observed throughout the entire, micrometer-thick MgO films. A further major result is the recognition of the substantial impact the substrate temperature and the ballistic deposition rate during the deposition process have on the films obtained. Just by changing the deposition temperature, it is possible to generate two different types of MgO films: compact, light-yellow films ($T_S = -190$ °C) with an excess of oxygen atoms surrounding small rock salt type MgO crystallites, and columnar, white films ($T_S = 25$ °C) exhibiting a superfilled rock salt structure. Furthermore, these results demonstrate the impact of the high ballistic depositions rates, which are essential for the stabilization of the dioxygen species within the MgO films. These insights open up new prospects for fine-tuning the properties of such films and enhance the performance of devices employing MgO films, such as the textured MgO buffer layers employed in the fabrication of tapes made of high-temperature superconductors for use in coils, which are prepared by a ballistic deposition process [86].

Supplementary Materials: The following supporting information can be downloaded at: https://www.mdpi.com/article/10.3390/coatings14121563/s1, Figures S1–S5; data of different (hypothetical) calculated MgO structures and Table S1 (calculated Raman wavenumbers of MgO structures).

Author Contributions: Conceptualization, D.F.; methodology, D.F.; validation, D.F., D.Z., K.K. and J.C.S.; visualization, D.F.; investigation (sample preparation, XRD, Rietveld, Raman), D.F.; investigation (DFT-calculations), D.Z.; investigations (XPS-Investigation), K.K.; data curation, D.F. and K.K.; writing—original draft, D.F.; writing—review and editing, D.F., D.Z., K.K. and J.C.S. All authors have read and agreed to the published version of the manuscript.

Funding: This research received no external funding.

Institutional Review Board Statement: Not applicable.

Informed Consent Statement: Not applicable.

Data Availability Statement: The datasets generated and/or analyzed during the current study are not publicly available but are available from the corresponding author on reasonable request.

Acknowledgments: We gratefully acknowledge helpful technical support by B. Fenk and U. Waizmann for the SEM and EDX measurements at the Max Planck Institute for Solid State Research.

Conflicts of Interest: The authors declare no conflicts of interest.

References

1. Adachi, S. Magnesium Oxide (MgO). In *Optical Constants of Crystalline and Amorphous Semiconductors*; Springer: Boston, MA, USA, 1999; pp. 411–419.
2. D'Ans, J.; Lax, E. *Taschenbuch für Chemiker und Physiker*, 3rd ed.; Springer: Berlin/Heidelberg, Germany, 1967; p. 415.
3. Tsirel'son, V.G.; Avilov, A.S.; Abramov, Y.A.; Belokoneva, E.L.; Kitaneh, R.; Feil, D. X-ray and Electron Diffraction Study of MgO. *Acta. Crystallogr. B* **1998**, *54*, 8–17. [CrossRef]
4. Yuan, H.T.; Liu, Y.Z.; Zeng, Z.Q.; Mei, Z.X.; Guo, Y.; Zhang, P.; Du, X.L.; Jia, J.F.; Zhang, Z.; Xue, Q.K. Formation of metastable MgO structures on type-III oxide surfaces: Effect of periodic out-of-plane electric dipole moment of substrates. *J. Cryst. Growth* **2009**, *311*, 425–428. [CrossRef]
5. Stachowicz, M.; Wierzbicka, A.; Sajkowski, J.M.; Pietrzyk, M.A.; Dluzewski, P.; Dynowska, E.; Dyczewski, J.; Morawiec, K.; Kryvyi, S.B.; Magalhaes, S.; et al. Structural analysis of the ZnO/MgO superlattices on a-polar ZnO substrates grown by MBE. *Appl. Surf. Sci.* **2022**, *587*, 152830. [CrossRef]
6. Martínez-Boubeta, C.; Botana, A.S.; Pardo, V.; Baldomir, D.; Antony, A.; Bertomeu, J.; Rebled, J.M.; López-Conesa, L.; Estradé, S.; Peiró, F. Heteroepitaxial growth of MgO(111) thin films on Al_2O_3(0001): Evidence of a wurtzite to rocksalt transformation. *Phys. Rev. B* **2012**, *86*, 041407(R). [CrossRef]
7. Schön, J.C.; Jansen, M. Determination of candidate structures for simple ionic compounds through cell optimization. *Comput. Mater. Sci.* **1995**, *4*, 43–58. [CrossRef]
8. Schön, J.C. Nanomaterials—What energy landscapes can tell us. *Proc. Appl. Ceram.* **2015**, *9*, 157–168. [CrossRef]
9. Schön, J.C. Enthalpy Landscapes of the Earth Alkaline Metal Oxides. *Z. Anorg. Allg. Chem.* **2004**, *630*, 2354–2366. [CrossRef]
10. Tahmashi, H.; Goedecker, S.; Ghasemi, S.A. Large-scale structure prediction of near-stoichiometric magnesium oxide based on a machine-learned interatomic potential: Crystalline phases and oxygen-vacancy ordering. *Phys. Rev. Mater.* **2021**, *5*, 083806. [CrossRef]
11. Fernandes, M.; Singh, K.R.B.; Sarkar, T.; Singh, P.; Singh, R.P. Recent Applications Of Magnesium Oxide (MgO) Nanoparticles In Various Domains. *Adv. Mater. Lett.* **2020**, *11*, 20081543. [CrossRef]
12. Rohmawati, L.; Fathoni, S.N.; Setyarsih, W.; Putri, N.P.; Darminto, D. Irradiation Time Optimization on Photocatalytic Activity of Nanoparticles MgO from Dolomite Bangkalan. *Trends Sci.* **2024**, *21*, 7442. [CrossRef]
13. Dabhane, H.; Ghotekar, S.; Tambade, P.; Pansambal, S.; Oza, R.; Medhane, V. MgO nanoparticles: Synthesis, characterization, and applications as a catalyst for organic transformations. *Eur. J. Chem.* **2021**, *12*, 86–108. [CrossRef]
14. Corneille, J.S.; He, J.-W.; Goodman, D.W. XPS characterization of ultra-thin MgO films on a Mo(100) surface. *Surf. Sci.* **1994**, *306*, 269–278. [CrossRef]
15. Wollschläger, J.; Viernow, J.; Tegenkamp, C.; Erdös, D.; Schröder, K.-M.; Pfnür, H. Stoichiometry and morphology of MgO films grown reactively on Ag(100). *Appl. Surf. Sci.* **1999**, *142*, 129–134. [CrossRef]
16. Matsuzaki, K.; Takagi, H.; Hosono, H.; Susaki, T. Structural study of polar MgO(111) epitaxial thin films grown on $SrTiO_3$(111). *Phys. Rev. B* **2011**, *84*, 235448. [CrossRef]
17. Jin, Z.; Nori, S.; Lee, Y.-F.; Kumar, D.; Wu, F.; Prater, J.T.; Kim, K.W.; Narayan, J. Strain induced room temperature ferromagnetism in epitaxial magnesium oxide thin films. *J. Appl. Phys.* **2015**, *118*, 165309. [CrossRef]
18. Craft, H.S.; Ihlefeld, J.F.; Losego, M.D.; Collazo, R.; Sitar, Z.; Maria, J.-P. MgO epitaxy on GaN (0002) surfaces by molecular beam epitaxy. *Appl. Phys. Lett.* **2006**, *88*, 212906. [CrossRef]

19. Goodrich, T.L.; Chai, Z.; Ziemer, K.S. Stability of MgO(1 1 1) films grown on 6H-SiC(0 0 0 1) by molecular beam epitaxy for two-step integration of functional oxides. *Appl. Surf. Sci.* **2008**, *254*, 3191–3199. [CrossRef]
20. Kerrigan, A.; Pande, K.; Pingstone, D.; Cavill, S.A.; Gajdardziska-Josifovska, M.; McKenna, K.P.; Weinert, M.; Lazarov, V.K. Nano-faceted stabilization of polar-oxide thin films: The case of MgO(111) and NiO(111) surfaces. *Appl. Surf. Sci.* **2022**, *596*, 153490. [CrossRef]
21. Goodrich, T.L.; Cai, Z.; Losego, M.D.; Maria, J.-P.; Ziemer, K.S. Thin, crystalline MgO on hexagonal 6H- Si C (0001) by molecular beam epitaxy for functional oxide integration. *J. Vac. Sci. Technol. B* **2007**, *25*, 1033–1038. [CrossRef]
22. Oliver, J.B.; Smith, C.; Spaulding, J.; Rigatti, A.L.; Charles, B.; Papernov, S.; Taylor, B.; Foster, J.; Carr, C.W.; Luthi, R.; et al. Glancing-angle–deposited magnesium oxide films for high-fluence applications. *Opt. Mater. Express* **2016**, *6*, 2291. [CrossRef]
23. Dohnalek, Z.; Kimmel, G.A.; McCready, D.E.; Young, J.S.; Dohnalkova, A.; Smith, R.S.; Kay, B.D. Structural and Chemical Characterization of Aligned Crystalline Nanoporous MgO Films Grown Via Reactive Ballistic Deposition. *J. Phys. Chem. B* **2002**, *106*, 3526–3529. [CrossRef]
24. Ma, B.; Li, M.; Jee, Y.A.; Koritala, R.E.; Fisher, B.L.; Balachandran, U. Inclined-substrate deposition of biaxially textured magnesium oxide thin films for YBCO coated conductors. *Phys. C* **2002**, *366*, 270–276. [CrossRef]
25. Stuart, S.C.; Satchet, E.; Sandin, A.; Maria, J.-P.; Rowe, J.E.; Dougherty, D.B.; Ulrich, M.J. Smooth MgO films grown on graphite and graphene by pulsed laser deposition. *Vac. Sci. Technol. B* **2013**, *31*, 051804. [CrossRef]
26. Kodu, M.; Raud, J.; Aints, M.; Avarmaa, T.; Denks, V.; Choi, J.-S.; Feldbach, E.; Jaaniso, R.; Kirm, M.; Lee, M.S.; et al. Structural and discharging properties of MgO thin films prepared by pulsed laser deposition. *Thin Solid Films* **2010**, *519*, 846–851. [CrossRef]
27. Wang, W.B.; Yang, Y.; Yanguas-Gil, A.; Chang, N.N.; Girolami, G.S.; Abelson, J.R. Highly conformal magnesium oxide thin films by low-temperature chemical vapor deposition from $Mg(H_3BNMe_2BH_3)_2$ and water. *Appl. Phys. Lett.* **2013**, *102*, 101605. [CrossRef]
28. Sung, M.M.; Kim, C.; Kim, C.G.; Kim, Y.J. Epitaxial growth of MgO films on Si(111) by metal organic chemical vapor deposition. *J. Cryst. Growth* **2000**, *210*, 651–654. [CrossRef]
29. Cáceres, D.; Colera, I.; Vergara, I.; González, R.; Román, E. Characterization of MgO thin films grown by rf-sputtering. *Vacuum* **2002**, *67*, 577–581. [CrossRef]
30. Singh, J.P.; Kumar, M.; Lin, W.C.; Lee, H.H.; Lee, Y.M.; Lee, S.; Chae, K.H. MgO Thin Film Growth on Si(001) by Radio-Frequency Sputtering Method. *J. Nanosci. Nanotechnol.* **2020**, *20*, 7530–7534. [CrossRef] [PubMed]
31. Kaneko, S.; Funakubo, H.; Kadowaki, T.; Hirabayashi, Y.; Akiyama, K. Cubic-on-cubic growth of a MgO(001) thin film prepared on Si(001) substrate at low ambient pressure by the sputtering method. *Europhys. Lett.* **2008**, *81*, 46001. [CrossRef]
32. Zhu, T.J.; Lu, L.; Zhao, X.B. Orientation of MgO thin films grown by pulsed laser deposition. *Mater. Sci. Engin. B* **2006**, *129*, 96–99. [CrossRef]
33. Maier, A.R.; Niu, F.; Wessels, B.W. Integration of $BaTiO_3$ on Si (001) using MgO/STO buffer layers by molecular beam epitaxy. *J. Cryst. Growth* **2006**, *294*, 401–406. [CrossRef]
34. Losego, M.D.; Craft, H.S.; Paisley, E.A.; Mita, S.; Collazo, R.; Sitar, Z.; Maria, J.-P. Critical examination of growth rate for magnesium oxide (MgO) thin films deposited by molecular beam epitaxy with a molecular oxygen flux. *J. Mater. Res.* **2010**, *25*, 670–679. [CrossRef]
35. Uddin, G.M.; Ziemer, K.S.; Zeid, A.; Lee, Y.-T.T.; Kamarthi, S. Process control model for growth rate of molecular beam epitaxy of MgO (111) nanoscale thin films on 6H-SiC (0001) substrates. *Int. J. Adv. Manuf. Technol.* **2017**, *91*, 907–916. [CrossRef]
36. Uddin, G.M.; Ziemer, K.S.; Zeid, A.; Kamarthi, S. Monte Carlo study of the molecular beam epitaxy process for manufacturing magnesium oxide nano-scale films. *IIE Trans.* **2015**, *47*, 125–140. [CrossRef]
37. Chambers, S.A.; Tran, T.T.; Hileman, T.A. Molecular beam homoepitaxial growth of MgO(001). *J. Mater. Res.* **1994**, *9*, 2944–2952. [CrossRef]
38. Geneste, G.; Morillo, J.; Finocchi, F.; Hayoun, M. Primary nucleation processes in binary oxide growth: The case of MgO. *Surf. Sci.* **2007**, *601*, 5616–5627. [CrossRef]
39. Kantorovich, L.N.; Gillan, M.J. Adsorption of atomic and molecular oxygen on the MgO (001) surface. *Surf. Sci.* **1997**, *374*, 373–386. [CrossRef]
40. Geneste, G.; Hayoun, M.; Finocchi, F.; Morillo, J. Competing mechanisms in the atomic diffusion of a MgO admolecule on the MgO(001) surface. *J. Phys. Condens. Matt.* **2009**, *21*, 315004. [CrossRef] [PubMed]
41. Kubo, M.; Oumi, Y.; Miura, R.; Fahmi, A.; Stirling, A.; Kawasaki, M.; Yoshimoto, M.; Koinuma, H. Layer-by-layer homoepitaxial growth process of MgO(001) as investigated by molecular dynamics, density functional theory, and computer graphics. *J. Chem. Phys.* **1997**, *107*, 4416–4422. [CrossRef]
42. Singh, J.P.; Chae, K.H. d° Ferromagnetism of Magnesium Oxide. *Condens. Matter.* **2017**, *2*, 36. [CrossRef]
43. Araujo, C.M.; Kapilashrami, M.; Jun, X.; Jayakumar, O.D.; Nagar, S.; Wu, Y.; Århammar, C.; Johansson, B.; Belova, L.; Ahuja, R.; et al. Room temperature ferromagnetism in pristine MgO thin films. *Appl. Phys. Lett.* **2010**, *96*, 232505. [CrossRef]
44. Li, J.; Jiang, Y.; Li, Y.; Yang, D.; Xu, Y.; Yan, M. Origin of room temperature ferromagnetism in MgO films. *Appl. Phys. Lett.* **2013**, *102*, 072406.
45. Kapilashrami, M.; Xu, J.; Rao, K.V.; Belova, L.; Carlegrim, E.; Fahlman, M. Experimental evidence for ferromagnetism at room temperature in MgO thin films. *J. Phys. Condens. Matter.* **2010**, *22*, 345004. [PubMed]

46. Wang, M.; Tang, S.; Hou, D.; Meng, F.; Han, Y.; Ren, J.; Wang, B.; Zhou, T. Possible origin of ferromagnetism in pristine magnesium oxide film. *Phys. B* **2020**, *590*, 412214.
47. Hazarika, R.; Kalita, B. Electronic structure alteration in MgO monolayer through alkali metal doping. *Mater. Today Proc.* **2023**, *4*, 619. [CrossRef]
48. Van On, V.; Guerrero-Sanchez, J.; Ponce-Pérez, R.; Vu, T.V.; Rivas-Silva, J.F.; Cocoletzi, G.H.; Hoat, D.M. Defective and doped MgO monolayer as promising 2D materials for optoelectronic and spintronic applications. *Mater. Sci. Semicond. Process* **2022**, *149*, 106876.
49. Benedetti, S.; Nilius, N.; Torelli, P.; Renaud, G.; Freund, H.-J.; Valeri, S. Competition between Polar and Nonpolar Growth of MgO Thin Films on Au(111). *J. Phys. Chem. C* **2011**, *115*, 23043–23049.
50. Smith, D.L. *Thin Film Deposition: Principles and Practice*; McGraw-Hill: New York, NY, USA, 1995; pp. 94–98.
51. Coelho, A.A. TOPAS and TOPAS-academic. *J. Appl. Cryst.* **2018**, *51*, 210–218.
52. Fischer, D.; Zagorac, D.; Schön, J.C. Fundamental Insight Into the Formation of the Zinc Oxide Crystal Structure. *Thin Solid Films* **2023**, *782*, 140017. [CrossRef]
53. Bergerhoff, G.; Berndt, M.; Brandenburg, K. Evaluation of Crystallographic Data with the Program DIAMOND. *J. Res. Natl. Inst. Stand. Technol.* **1996**, *101*, 221–225. [PubMed]
54. Fischer, D.; Zagorac, D.; Schön, J.C. The Presence of Superoxide Ions and Related Dioxygen Species in Zinc Oxide—A Structural Characterization by In-Situ Raman Spectroscopy. *J. Raman Spectrosc.* **2022**, *53*, 2137–2146.
55. Biesinger, M.C. Accessing the robustness of adventitious carbon for charge referencing (correction) purposes in XPS analysis: Insights from a multi-user facility data review. *Appl. Surf. Sci.* **2022**, *597*, 153681.
56. Fairley, N.; Fernandez, V.; Richard-Plouet, M.; Guillot-Deudon, C.; Walton, J.; Smith, E.; Flahaut, D.; Greiner, M.; Biesinger, M.; Tougaard, S.; et al. Systematic and collaborative approach to problem solving using X-ray photoelectron spectroscopy. *Appl. Surf. Sci. Adv.* **2021**, *5*, 100112.
57. Scofield, J.H. Hartree-Slater subshell photoionization cross-sections at 1254 and 1487 eV. *J. Electron Spectros. Relat. Phenom.* **1976**, *8*, 129–137. [CrossRef]
58. Dovesi, R.; Erba, A.; Orlando, R.; Zicovich-Wilson, C.M.; Civalleri, B.; Maschio, L.; Rérat, M.; Casassa, S.; Baima, J.; Salustro, S.; et al. Quantum-mechanical condensed matter simulations with CRYSTAL. *WIREs Comput. Mol. Sci.* **2018**, *8*, e1360.
59. Hundt, R. *KPLOT: A Program for Plotting and Analysing Crystal Structures*; Technicum Scientific Publishing: Stuttgart, Germany, 2016.
60. Pascale, F.; Zicovich-Wilson, C.M.; Gejo, F.L.; Civalleri, B.; Orlando, R.; Dovesi, R. The calculation of the vibrational frequencies of crystalline compounds and its implementation in the CRYSTAL code. *J. Comput. Chem.* **2004**, *25*, 888.
61. Ferrero, M.; Rerat, M.; Orlando, R.; Dovesi, R.; Bush, I.J. Coupled perturbed Kohn-Sham calculation of static polarizabilities of periodic compounds. *J. Phys. Conf. Ser.* **2008**, *117*, 012016. [CrossRef]
62. Becke, A.D. Density-functional thermochemistry. III. The role of exact exchange. *J. Chem. Phys.* **1993**, *98*, 5648–5652.
63. Perdew, J.P.; Burke, K.; Ernzerhof, M. Generalized Gradient Approximation Made Simple. *Phys. Rev. Lett.* **1996**, *77*, 3865–3868. [PubMed]
64. Buyer, C.; Grossholz, H.; Wolf, S.; Zagorac, D.; Zagorac, J.; Schön, J.C.; Schleid, T. Crystal-Structure Prediction and Experimental Investigation of the Polymorphic Lanthanum Fluoride Selenides LaFSe and La_2F_4Se. *Cryst. Growth Des.* **2022**, *22*, 7133–7142.
65. Valenzano, L.; Noel, Y.; Orlando, R.; Zicovich-Wilson, C.M.; Ferrero, M.; Dovesi, R. Ab initio vibrational spectra and dielectric properties of carbonates: Magnesite, calcite and dolomite. *Theor. Chem. Acc.* **2007**, *117*, 991–1000. [CrossRef]
66. Zagorac, D.; Schön, J.C.; Zagorac, J.; Jansen, M. Prediction of structure candidates for zinc oxide as a function of pressure and investigation of their electronic properties. *Phys. Rev. B* **2014**, *89*, 075201. [CrossRef]
67. Gatta, G.D.; Nestola, F.; Bromiley, G.D.; Loose, A. New insight into crystal chemistry of topaz: A multi-methodological study. *Am. Mineral.* **2006**, *91*, 1839–1846. [CrossRef]
68. Rosengarten, C.A.; Yuvaraj, K.; Lim, L.F.; Cox, N.; Jones, C. Ketyl Radicals Generated from Magnesium(I) Compounds: Useful Reagents for C−C Bond Forming Reactions. *Chem. Eur. J.* **2023**, *29*, e202300135. [CrossRef]
69. Emsley, J. *The Elements*; Clarendon Press: Oxford, UK, 1998; p. 134.
70. Ono, S.; Ishido, Y.; Imanari, K.; Tabata, T.; Cho, Y.K.; Yamamoto, R.; Doyama, M. Phase transformation and thermal expansion of Mg-Ni alloys in a hydrogen atmosphere. *J. Less-Common. Met.* **1982**, *88*, 57–61. [CrossRef]
71. Green, S.P.; Jones, C.; Stasch, A. Stable Magnesium(I) Compounds with Mg-Mg Bonds. *Science* **2007**, *318*, 1754–1757. [CrossRef]
72. Karki, B.B.; Wentzcovitch, R.M.; de Gironcoli, S.; Baroni, S. High-pressure lattice dynamics and thermoelasticity of MgO. *Phys. Rev. B.* **2000**, *61*, 8793–8800. [CrossRef]
73. Dekermenjian, M.; Ruediger, A.P.; Merlen, A. Raman spectroscopy investigation of magnesium oxide nanoparticles. *RSC Adv.* **2023**, *13*, 26683–26689. [CrossRef] [PubMed]
74. Manson, N.B.; der Qhe, Y.; Chodos, S.L. Second-Order Raman Spectrum of MgO. *Phys. Rev. B* **1971**, *3*, 1968–1972. [CrossRef]
75. Hatzenbuhler, D.A.; Andrews, L. Raman and Infrared Spectra of LiO_2 in Oxygen Matrices. *J. Chem. Phys.* **1972**, *56*, 3398–3403. [CrossRef]
76. Eysel, H.H.; Thym, S. Raman Spectra of Peroxides. *Z. Anorg. Allg. Chem.* **1975**, *411*, 97–102. [CrossRef]
77. Lobanov, S.S.; Zhu, Q.; Holtgrewe, N.; Prescher, C.; Prakapenka, V.B.; Oganov, A.R.; Goncharov, A.F. Stable magnesium peroxide at high pressure. *Sci. Rep.* **2015**, *5*, 13582. [CrossRef] [PubMed]

78. Tuschel, D. Selecting an Excitation Wavelength for Raman Spectroscopy. *Spectroscopy* **2016**, *31*, 14–23.
79. Vasquez, R.P. MgO(100) by XPS. *Surf. Sci. Spectra* **1993**, *2*, 13–19. [CrossRef]
80. Peterka, D.; Tegenkamp, C.; Schröder, K.-M.; Ernst, W.; Pfnür, H. Oxygen surplus and oxygen vacancies on the surface of epitaxial MgO layers grown on Ag(100). *Surf. Sci.* **1999**, *431*, 146–155. [CrossRef]
81. Casey, P.; Hughes, G.; Connor, E.O.; Long, R.D.; Hurley, P.K. Growth and Characterisation of Thin MgO Layers on Si(100) surfaces. *J. Phys.* **2008**, *100*, 042046. [CrossRef]
82. Kim, C.M.; Jeong, H.S.; Kim, E.H. NEXAFS and XPS characterization of molecular oxygen adsorbed on Ni(100) at 80 K. *Surf. Sci.* **2000**, *459*, L457–L461. [CrossRef]
83. Mg-O Distance Range for Tetrahedral Coordinated Magnesium Based on the Crystal Data of the Following Compounds: MgAl2O4, MgV2O4, MgCr2O4, MgFe2O4, MgMn2O4, MgSiO3, Mg2TiO4, Mg3Nb6O11, Mg3(PO4)2 Taken from PDF4+ Database of ICDD 2022, PA, USA, Software Version 4.22.0.2. Available online: https://www.icdd.com (accessed on 28 October 2024).
84. Kjekshus, A.; Rakke, T. Preparation and Properties of Magnesium, Copper, Zinc and Cadmium Dichalcogenides. *Acta Chem. Scan. A* **1979**, *33*, 617–620. [CrossRef]
85. Wang, Z.L.; Bentley, J.; Kenik, E.A.; Horton, L.L.; McKee, R.A. In-situ formation of MgO, thin films on MgO single-crystal surfaces at high temperatures. *Surf. Sci.* **1992**, *273*, 88–108. [CrossRef]
86. Sigl, G. Herstellung von Technischen Substraten Mit Biaxial Texturierten Pufferschichten für Supraleitende Bandleiter der 2. Generation. Ph.D. Thesis, Technische Universität München, Fakultät für Physik, München, Germany, 2009; pp. 72–74.
87. Geneste, G.; Morillo, J.; Finocchi, F.J. Adsorption and diffusion of Mg, O, and O_2 on the MgO(001) flat surface. *Chem. Phys.* **2005**, *122*, 174707. [CrossRef]
88. Yadavalli, S.; Yang, M.H.; Flynn, C.P. Low-temperature growth of MgO by molecular-beam epitaxy. *Phys. Rev. B* **1990**, *41*, 7961–7964. [CrossRef]
89. Toto, N.; Schön, J.C.; Jansen, M. Atomistic study of xenon crystal growth via low-temperature atom beam deposition. *Phys. Rev. B* **2010**, *82*, 115401. [CrossRef]
90. Meng, H.; Kuzovnikov, M.A.; Tkacz, M. Phase stability of some rare earth trihydrides under high pressure. *Int. J. Hydrogen Energy* **2017**, *42*, 29344–29349. [CrossRef]
91. Lazicki, A.; Maddox, B.; Evans, W.J.; Yoo, C.-S.; McMahan, A.K.; Pickett, W.E.; Scalettar, R.T.; Hu, M.Y.; Chow, P. New Cubic Phase of Li_3N: Stability of the N^{3-} Ion to 200 GPa. *Phys. Rev. Lett.* **2005**, *95*, 165503. [CrossRef] [PubMed]
92. Vajenine, G.V.; Wang, X.; Efthimiopoulos, I.; Karmakar, S.; Syassen, K.; Hanfland, M. Structural phase transitions of sodium nitride at high pressure. *Phys. Rev. B* **2009**, *79*, 224107. [CrossRef]
93. Greis, O.; Martinez-Ripoll, M. Darstellung, Temperaturverhalten und Kristallstruktur von BiF_3. *Z. Anorg. Allg. Chem.* **1977**, *436*, 105–112. [CrossRef]